Research Article | Vol. 29, No. 2 / 18 January 2021 / Optics Express 1371
Optics EXPRESS

Modular microring laser cavity sensor

LANTIAN CHANG,* MICHIEL DE GOEDE, MEINDERT DIJKSTRA, CARLIJN I. VAN EMMERIK, AND SONIA M. GARCÍA-BLANCO

Optical Sciences Group, MESA+ Institute for Nanotechnology, University of Twente, P.O. Box 217, 7500 AE Enschede, The Netherlands
l.chang@utwente.nl

Abstract: We propose and experimentally demonstrate a modular microring laser (MML) cavity for sensing applications. The proposed MML permits much more design freedom compared with a traditional simple ring cavity by decoupling the performance parameters into several regions in the cavity. Thus, the different biosensor performance parameters can be optimized semi-independently limiting the need for trade-offs on the design of the biosensing device. The first generation MML has been fabricated and tested. A fiber-to-fiber slope efficiency of up to 1.2%, a temperature coefficient of 1.35 GHz/K and a 3σ limit of detection (LOD) of 3.1×10^{-7} RIU without averaging and 6.0×10^{-8} RIU with a 60 s averaging, has been measured for the MML sensor, which is a record-low LOD in on-chip ring cavity optical sensors. Further optimization is possible, capitalizing on the key advantage of the MML concept, namely the potential for designing the laser cavity to achieve the desired optimization goals.

1. Introduction

Whispering gallery mode (WGM) based optical sensors have been widely studied due to their high sensitivity for the label-free detection of biomarkers [1–4]. The full-width half maximum (FWHM) of the resonances, their mode splitting and their frequency shift are parameters that can be used to detect nanoparticles or molecules attaching to the surface of the resonator [3,5,6]. The frequency shift method can be applied in both passive and active (lasing) cavities. The lasing cavities have several advantages over the passive ones. First, the intrinsic minimal detectable shift, thus the lower detection limit, is proportional to the resonance linewidth [7], which is much narrower in an active resonator. Second, a passive cavity resonance shift is typically measured with an optical spectrum analyzer (OSA) or tunable laser, while a lasing cavity resonance can be characterized with a RF spectrum analyzer in a heterodyne detection configuration [8]. Since typical RF spectrum analyzers can measure with much smaller frequency step size than OSAs and tunable lasers, a higher resolution in the frequency shift measurement, and consequently, a lower measurable limit of detection (LOD) can be achieved.

Many active sensors have been developed [8–14]. Typically optical pumping is preferred over electrical pumping to prevent the difficulties to operate an electrically pumped laser cavity in a liquid environment. However, the proposed active sensors have limitations on performance optimization, multiplexing (i.e., several sensors integrated on a same module to detect an array of analytes), and mass production due to their delicate free-space configuration or their fragile light coupling scheme. Integrated photonic waveguide based active biosensors [15–18] could overcome the above mentioned limitations. Our previous work [16–18] demonstrates optically pumped active biosensors based on Al_2O_3:Yb^{3+} integrated microdisk resonators. However, the design challenge of such a microdisk based active biosensor is the entanglement of performance parameters. In order to exploit the full potential of an active sensor, it would be desirable to have more degrees of freedom in the design to independently optimize performance parameters such as sensitivity, efficiency and free spectral range (FSR).

#411811 https://doi.org/10.1364/OE.411811
Journal © 2021 Received 15 Oct 2020; revised 15 Dec 2020; accepted 21 Dec 2020; published 8 Jan 2021

Optics EXPRESS

In this work, we propose a modular microring laser (MML) cavity design that minimizes the entanglement and trade-off between the different performance parameters. With the proposed approach, optimizing an active sensor for a particular performance goal can be achieved in a systematic way. On particular, we are interested in optimizing simultaneously the LOD and the power efficiency. The proposed design methodology of the MML is discussed in detail. The implementation in the Al_2O_3:Yb^{3+} integrated photonic platform is then detailed. The fabrication and characterization of the first Al_2O_3:Yb^{3+} MML device is presented. The measured lasing power, temperature coefficient and LOD exhibit considerable improvement with respect to the active sensor based on a simple microdisk geometry of our earlier work [18].

2. Cavity design

In subsection 2.1, we first describe the challenges that arise when designing an optically pumped simple microring /microdisk laser for biosensing applications. In order to overcome these challenges, we propose a cavity with a modular design, an MML, in subsection 2.2. The detailed design methodology is then described and applied to the development of an active sensor in the Al_2O_3:Yb^{3+} integrated photonic platform.

2.1. Active microring/microdisk cavity sensor: design challenges

Figure 1(a) shows an optically pumped traditional simple microring laser cavity. There are 4 geometrical parameters, namely waveguide thickness (*H*), waveguide width (*W*), ring radius (*R*), and gap (*G*), which can be tuned to achieve certain design goals. However, each of those geometrical parameters is entangled with multiple performance parameters and vice versa, as shown in Table 1. For instance, to optimize for sensitivity, the waveguides should be made as thin and narrow as possible. However, this increases bend losses and coupling of the laser wavelength to the bus waveguide resulting in an increased laser threshold and even compromised lasing. In practice, it is difficult to design a ring cavity with improved sensitivity and power efficiency at the same time.

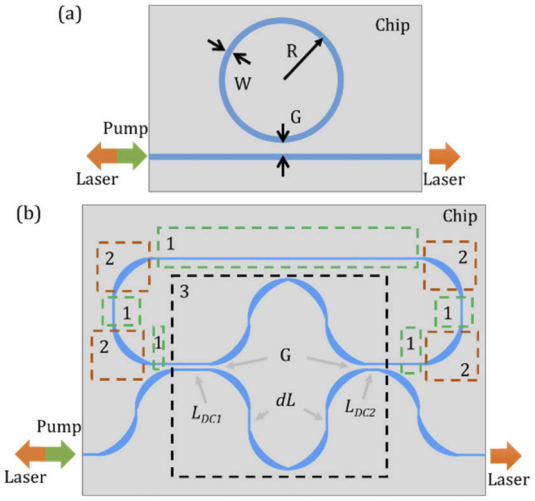

Fig. 1. (a) Optically pumped simple microring laser. (b) Proposed optically pumped MML cavity architecture. Dashed boxes indicate 3 different kinds of regions that are used to adjust performance parameters in a quasi-independent manner.

Optics EXPRESS

Table 1. Relation between geometrical parameters and performance parameters in a simple ring design

Increasing H, W, R, G	H	W	R	G
1. Sensitivity	↓	↓	—[a]	—[b]
2. Pump wavelength coupling (not in resonance)	↓	↓	↑	↓
3. Lasing wavelength coupling	↓	↓	↑	↓
4. Bend loss	↓	↓	↓	—[b]
5. Lasing threshold	↑ or ↓[c]	↑ or ↓[c]	↑ or ↓[d]	↑ or ↓[e]
6. Slope efficiency	↑ or ↓[e]	↑ or ↓[e]	↑	↓
7. Lasing wavelength	↑ or ↓[f]	↑ or ↓[f]	↑ or ↓[f]	↑ or ↓[f]
8. FSR	↓	↓	↓	—[b]

H: Waveguide thickness; W: Waveguide width; R: Ring radius; G: Gap between the ring and the bus waveguide; ↑: Increase; ↓: Decrease.
The power coupling between the bus waveguide and the ring are considered to be a few percent for both pump and lasing wavelength. The pump is not in resonance with the ring.
[a]Negligible influence for the R we used.
[b]No influence.
[c]Need many other cavity parameters all together to predict since the opposite influence of 2 with 3, 4 [19].
[d]Need many other cavity parameters all together to predict since the opposite influence of 2 with 3 [19].
[e]Need many other cavity parameters all together to predict since the opposite influence of 2, 3 with 4 [19].
[f]Depends on the combination of the gain and loss spectra. The loss spectrum of the cavity modes depends on all the 4 geometric parameters [19].

2.2. MML design

The aim of the proposed modular architecture is to significantly improve the number of degrees of freedom on the design of a sensor cavity. Our strategy is to separate each performance parameter to a different section of the laser cavity. In this study, the Al_2O_3:Yb^{3+} waveguide platform is utilized as an example to demonstrate the complete process. The pump wavelength is 976 nm and the emission wavelength lies within the range ~1005 nm – 1060 nm.

The proposed MML design is shown in Fig. 1(b). The overall idea is to split the cavity into 3 regions that can be designed and optimized independently. Region 1 consist of straight waveguides and it is used to tune the sensitivity and the FSR. Region 2 consist of adiabatic (AD) bends designed to minimize the bend loss inside the cavity while keeping it as small as possible. Region 3 is a wavelength-division multiplexer (WDM) that consists of two directional couplers (DCs) and a Mach–Zehnder interferometer. The WDM is aimed to improve the power efficiency of the laser by providing a high pump wavelength coupling efficiency (into the cavity) and a designable lasing wavelength coupling efficiency (out of the cavity). In our current technology, however, these regions share the same waveguide thickness and therefore, their geometrical shape cannot be fully independently adjustable. The correct design order is key to minimize conflict imposed by the shared waveguide thickness. Therefore, we propose a 6-step design methodology to define all parameters one by one, and the details are listed in Table 2. Since the laser lases in the fundamental TE mode due to the lower bending loss for TE polarization, all simulations and experiments in this study are carried out for TE polarization.

In step 1 (Table 2), the goal is to design the cavity with high sensitivity to bulk refractive index changes in the H_2O flowing over the sensor. The fraction of the mode power in the H_2O, η, should be as high as possible for an increased sensitivity. A smaller core size pushes the evanescent field into the H_2O cladding thereby increasing the sensitivity. Waveguides with different core sizes have been simulated (n_{Al2O3} = 1.69 at 1030 nm) and their fundamental TE modes are shown in Fig. 2. A width of 1 μm was therefore selected, which is the minimum width that can be reliably fabricated with the UV contact lithography system used in this work (i.e., an EVG620 contact

Optics EXPRESS

mask aligner). The waveguide thickness is set in the step 2 (Table 2), where the bend loss is considered.

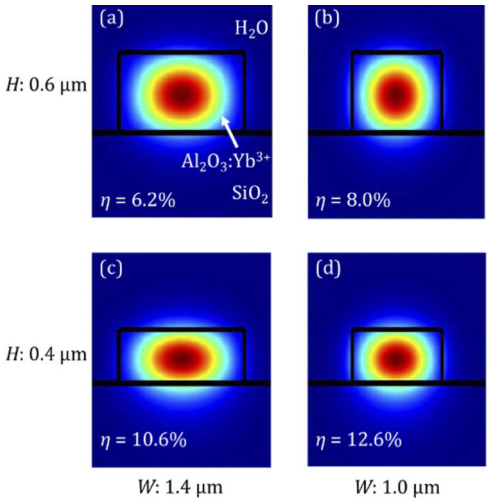

Fig. 2. Waveguide TE mode (wavelength of 1030 nm) simulation at different core height H and width W. The fraction of the power in H_2O is indicated with η. (a) Height 0.6 μm, width 1.4 μm. (b) Height 0.6 μm, width 1.0 μm. (c) Height 0.4 μm, width 1.4 μm. (d) Height 0.4 μm, width 1.0 μm.

Table 2. MML design procedure

Design steps	Design geometric parameters	Aimed performance parameters
1	Region 1: Waveguide width	Sensitivity
2	Region 2: Waveguide thickness and the AD bend design	Sensitivity and bend loss
3	Region 3: Arm length difference in the WDM	Define the pump and lasing wavelength
4	Region 3: Gap size of the two directional couplers of the WDM	—[a]
5	Region 3: Length of the two directional couplers of the WDM	Define the pump and lasing coupling efficiency independently.
6	Region 1: Waveguide length	FSR

[a]Negligible influence on all performance parameters aimed in this work. It should not be too large to prevent increasing the cavity size (footprint) significantly.

In step 2 (Table 2), the goal is to design the bends in the cavity. Thin waveguides favor sensitivity but limit the minimum bend radius that can be used to keep the overall losses of the cavity low thus keeping the laser threshold low and the slope efficiency high. The goal is to find a balance between the cavity size and the sensitivity by choosing the waveguide thickness and designing the bend shape. We selected a height of 0.4 μm, favorable to increase sensitivity. The AD bends are then designed to keep the overall cavity losses as low as possible. Prior to the AD bend design, bend (with constant radius and width) loss simulation is performed to provide essential information for the AD bend design parameters, such as the minimum bend radius within the adiabatic bend. Bend loss of a waveguide with a height of 0.4 μm and a width of 1.0 μm is simulated at the wavelength of 1060 nm as a function of bend radius (Fig. 3(a)). A bend loss of ~0.1 dB/cm, which is much smaller than the typical ~0.5 dB/cm propagation loss

Optics EXPRESS

of the waveguides, is set as design target to determine the minimum bend radius. This target corresponds to a bend radius of 230 μm for the selected 0.4 μm × 1 μm cross-section of the waveguides. The minimum radius can be further reduced by increasing the waveguide width (Fig. 3(b)). For example, a bend loss below 0.1 dB/cm can be reached with a bend radius as small as 75 μm when using a waveguide 3 μm wide. The connection between a 3 μm wide bend and a 1 μm straight waveguide is described below.

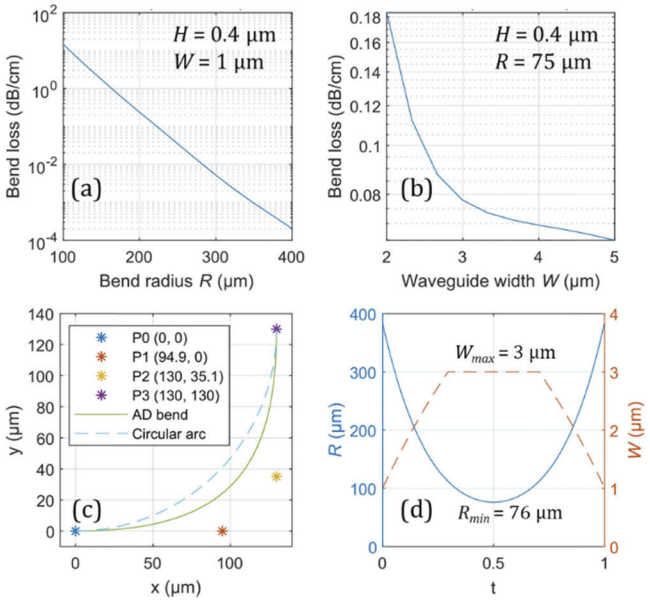

Fig. 3. (a) Bend loss (bend with constant radius and width) as a function of bend radius for a waveguide 0.4 μm high and 1 μm wide at a wavelength of 1060 nm. (b) Bend loss (bend with constant radius and width) as a function of waveguide width for a bend radius of 75 μm and 0.4 μm height at wavelength of 1060 nm. (c) The center path of an AD bend defined by a third-order Bezier curve compared with a circular arc with a radius of 130 μm. The ending positions of these two curves are the same. P0, P1, P2, and P3 are the control points of the third-order Bezier curve. (d) The radius of curvature, R, and waveguide width, W, of the AD bend shown in (c), where the t ($0 \leqslant t \leqslant 1$) is a parameter that indicates the normalized position along the AD bend. An FDTD simulation of this AD bend indicates a low loss of 0.006 dB/bend (including the straight to bend coupling loss at each side).

In order to have a lossless connection between a straight waveguide and bend waveguide an AD bend [20] is needed. An AD bend is a bend that starts with a very large bend radius at the connection point to a straight waveguide to ensure a negligible straight-to-bend coupling loss. It then gradually reduces its radius to a minimal value and reverses in the second half of the bend. The waveguide width in an AD bend can slowly increase as the bend radius decreases to further reduce the bend loss. Many curve functions and waveguide width changes have been explored in the literature [20–24] and in principle they can all be adapted and applied to the AD bend in this design. A relatively simple third order Bezier curve with linear waveguide width change are chosen for our cavity design. The shape and radius of curvature of a third order Bezier curve is controlled by 4 control points, P0, P1, P2, and P3, shown in Fig. 3(c). The waveguide width increases linearly as the bend radius decreases, as shown in Fig. 3(d). An FDTD simulation of the full AD bend indicates a low loss of 0.006 dB/bend (including the straight to bend coupling loss at each side).

Optics EXPRESS

In step 3 (Table 2), the goal is to maximize the efficiency of the laser by means of a WDM coupler (i.e., region 3 in Fig. 1(b)). The purpose of introducing a WDM in the device is to achieve a high pump coupling into the cavity (i.e., pump wavelength is 976 nm) simultaneously with a low laser wavelength coupling (i.e., the lasing wavelength ranges from ~1005-1060 nm), therefore obtaining a high Q cavity at the signal wavelength. In this example, the WDM is based on a Mach-Zehnder interferometer. The thickness and width of the waveguide have been defined in steps 1 and 2. The bends used in the WDM are the same bends as in region 2. Therefore, only the difference between the length of the two waveguides in the interferometer, dL, still needs to be defined. For the selected waveguide cross section, 1 μm wide and 0.4 μm thick, in the dL region, the simulated effective refractive indices are $n_{effp} = 1.4982$ and $n_{effl} = 1.4899$ for the pump (976 nm) and lasing (~1030 nm) wavelength, respectively. The phase delay difference can be set to $2\pi \cdot dL \cdot n_{effp}/\lambda_p = 2\pi \cdot M$ (where $M = 0, 1, 2, 3 \ldots$) for the pump and $2\pi \cdot dL \cdot n_{effl}/\lambda_l = 2\pi \cdot M - \pi$ for the desired lasing wavelength. By subtracting the two equations, $dL \cdot (n_{effl}/\lambda_l - n_{effp}/\lambda_p) = -0.5$ thus, $dL = 5.647$ μm. M can then be calculated by, $M = dL \cdot n_{effp}/\lambda_p \approx 8.7$ thus, round to $M = 9$. The pump wavelength has to be at 976 nm, but the lasing wavelength does not have to be 1030 nm, thus dL is recalculated to be $dL = M \cdot \lambda_p/n_{effp} = 5.863$ μm. The calculated minimal coupling wavelength is 1027.7 nm as shown in Fig. 4.

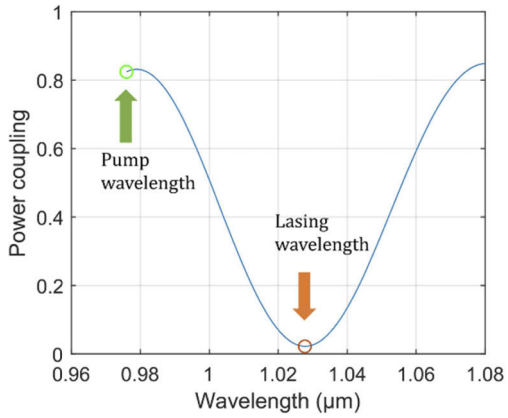

Fig. 4. Simulated WDM spectrum. An 82% pump coupling efficiency from the bus waveguide into the cavity (pump wavelength 976 nm) and 2% coupling at the lasing wavelength of 1027.7 nm can be achieved, leading to lasing at around 1027.7 nm. The parameters considered in this simulation are $G = 0.75$ μm (DC gap), $L_{DC1} = 103.6$ μm, $L_{DC1} = 85$ μm, $dL = 5.863$ μm and 1 μm wide, 0.4 μm thick waveguide for the dL region.

In step 4 (Table 2), the goal is to set the gap size of the two DCs in the WDM. This parameter is needed to simulate the length of the DC in the next step. In order to keep the DC as small as possible, a gap size of 0.75 μm, which is the smallest gap that can be reliably fabricated with UV contact lithography, is selected.

In step 5 (Table 2), the goal is to define the coupling efficiency of the WDM for both the pump and lasing wavelengths. The coupling efficiency of the pump is the sum of the two DCs. The coupling efficiency of the lasing wavelength is the difference of the two DCs. A WDM example has been simulated and it is shown in Fig. 4. In this example, the pump, at 976 nm, has 82% coupling efficiency into the laser cavity. The lasing wavelength, at 1027.7 nm, has 2.2% coupling efficiency from the cavity to the bus waveguide. Following this design methodology, the laser threshold and slope efficiency can be easily tuned by optimizing the pump and signal coupling efficiencies respectively.

Optics EXPRESS

In step 6 (Table 2), the goal is to tune the FSR of the cavity (if needed). The FSR has influence in different sensing performance parameters, such as the dynamic range and amount of mode-splitting (i.e., in sensors based on mode splitting). By connecting all the sections defined in steps 1-5, a minimal cavity size is defined, thus the maximal FSR. One can reduce the FSR by increasing the length of regions 1. The tuning of FSR will not influence the coupling spectrum of the WDM as long as the DCs are not changed. This is not possible in a normal simple microring cavity since the coupling changes with the ring radius.

In order to further improve the overall efficiency of the chip, a vertical taper is designed outside the laser cavity, as shown in Fig. 5. The thinner waveguide region has an enlarged mode size, which leads to higher coupling efficiency between the fiber and the waveguide. The enlarged mode size also has a reduced mode overlap with the doped waveguide core, thus limiting the absorption of the pump and the reabsorption of the emitted laser light in between the chip facet and the laser cavity. The fabrication of the taper is described in the following section.

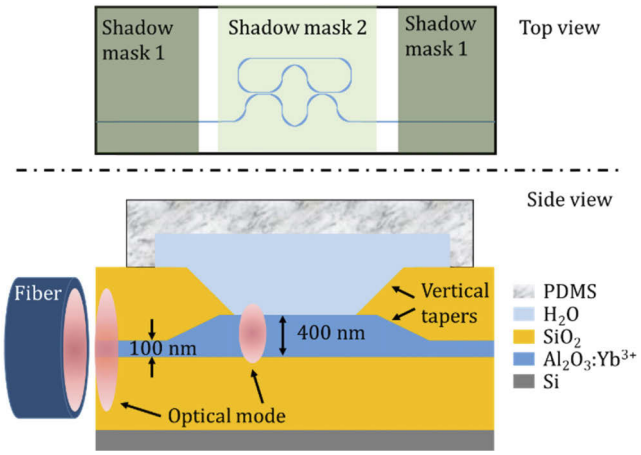

Fig. 5. Schematic of the fabricated device. The side view is aligned to the top view. The laser cavity is fabricated in the 400 nm thick Al_2O_3:Yb^{3+} region. The PDMS microfluidic channel is used to flow the liquid sample, in this work H_2O, on top of the laser cavity.

3. Fabrication

The device is fabricated in the MESA+ Nanolab cleanroom. The top and side view of the design is shown in Fig. 5. The key fabrication steps are described below and the detailed fabrication parameters for each step are described in our previous work [18]. The process starts with a Si wafer with an 8 µm thick thermal SiO_2 layer. A 100 nm thick Al_2O_3:Yb^{3+} layer (Yb^{3+} concentration: ~5×10^{20} cm^{-3}) is RF reactive co-sputtered with an AJA ATC 1500 on top of the thermal SiO_2 layer. Then a molybdenum shadow mask (mask 1 in Fig. 5) is placed on top of the wafer. Another 300 nm thick Al_2O_3:Yb^{3+} layer is deposited on the exposed region of the wafer [25]. A few hundreds of micrometers long slope in between the thin and thick region forms naturally due to the presence of the shadow mask. This region is long enough to act as an adiabatic vertical taper in between the thin and thick regions. A standard UV contact lithography (Olin OIR 906-12 resist, 1.2 µm thick) is then used to pattern the waveguides on both thin and thick Al_2O_3:Yb^{3+} regions simultaneously followed by reactive ion etching (Oxford PlasmaPro 100 Cobra) with BCl_3:HBr (5:2) using a total power of 25 W [26]. All 400 nm thick Al_2O_3:Yb^{3+} layer is etched through to create the channel waveguides. A plasma enhanced chemical vapor deposition (PECVD) SiO_2 top cladding (4 µm thick, deposited with Oxford Plasmalab 80 Plus at 300 C°) is then selectively deposited outside the laser cavity through a second shadow mask

Optics EXPRESS

(mask 2 in Fig. 5). After dicing, a temporary polydimethylsiloxane (PDMS) microfluidic channel is attached on top of the sensing window, which can then be filled with the sample liquid.

4. Experimental results

The lasing and sensing performance of the fabricated devices have been characterized. The results can be used as feedback for a next iteration in the optimization of the MML device.

4.1. Laser characterization

The setup utilized to characterize the lasing performance is shown in Fig. 6(a). The pump laser is a Thorlabs BL976-PAG700 followed by a fiber isolator (Thorlabs IO-J-980APC). The polarization maintaining (PM) WDM is an AFW WDM-PM-3098-L-P-7-1-1W. The residual pump power reaching the OSA from backscattering and backreflections via the PM WDM is well below -65 dBm. Therefore, when a power meter is used to measure the total lasing power, the contribution of the residual pump can be neglected.

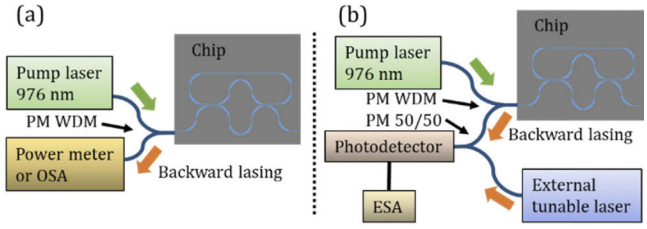

Fig. 6. (a) Lasing characterization setup. Pump light is sent into the chip through a PM fiber based WDM (980/1030 nm). The backward lasing light is coupled to a power meter (Coherent FieldMaxII) or OSA (Hewlett Packard 70950B, 0.5 nm resolution) via the PM fiber based WDM device. (b) Heterodyne sensing setup. A Toptica CTL1050 (external tunable laser, < 10 kHz linewidth) is heterodyned with one of the modes of the on-chip laser. The two lasers are combined together through a 1030 nm PM 50/50 fiber coupler (AFW PFC-30-2-50-L-P-7-1-FB-0.3W). The combined light is sent to a fast photodetector (New Focus 1014). A HP Agilent E4407B (1 kHz minimum resolution bandwidth) RF electrical spectrum analyzer (ESA) is used to measure the resulting beat note.

Images of lasing devices (top view) have been captured with a CMOS camera (FLIR BFLY-U3-23S6M-C) and they are shown in Fig. 7. Pump light is coupled into the bus waveguide from the left side. The camera is used to collect the scattered light from the waveguides, which is proportional to the light intensity inside the waveguides. The brightness in these images is approximately proportional to the pump power, since the pump power is much higher than the lasing power in these case and the camera has a higher sensitivity at the pump wavelength

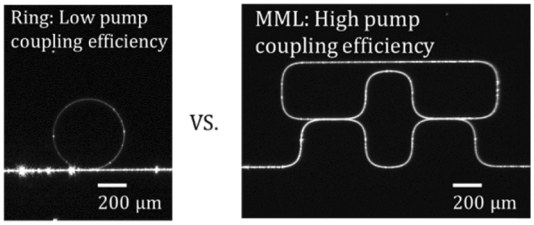

Fig. 7. Optical microscope images of a microring laser (left) versus an MML (right) during lasing. The relative brightness between the bus waveguide and the cavity indicates a higher pump coupling into the cavity with the MML design.

Optics EXPRESS

compared to the lasing wavelength. In case of a simple ring laser, the ring is clearly dimmer than the bus waveguide. This indicates low efficiency of the pump since only a small fraction of its intensity has been coupled from the bus waveguide into the microring laser cavity. On the other hand, the MML cavity has similar brightness as the bus waveguide, showing that most of the pump has passed through the cavity. The typical lasing power of this type of MML cavity is a factor 10 to 30 higher than that of the microring design for identical incident pump power. An example of the backward lasing power as a function of incident pump power (prior to coupling to the chip) is shown in Fig. 8.

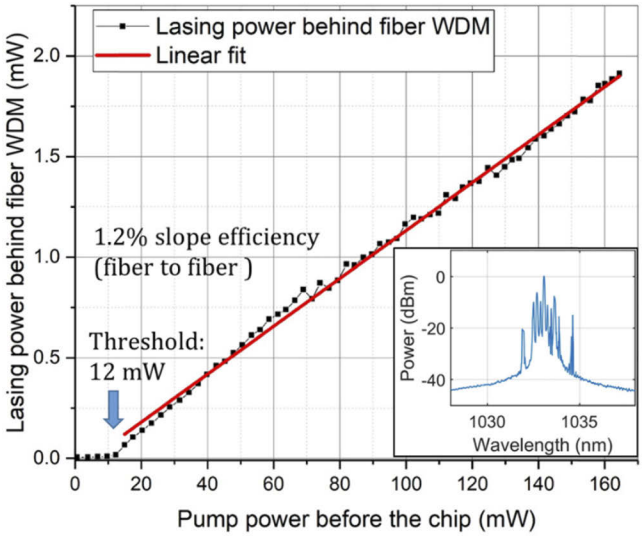

Fig. 8. Backward lasing power as a function of pump power. The pump power before the chip (incident pump power) is measured by replacing the chip with a power meter in Fig. 6(a). The backward lasing power behind the fiber WDM is measured by the power meter shown in Fig. 6(a) (which includes the losses of the WDM). The threshold pump power (incident) is 12 mW. A fiber-to-fiber slope efficiency of 1.2% has been measured. The on-chip slope efficiency is calculated to be $11 \pm 2\%$ based on a measured coupling efficiency of $33 \pm 3\%$. A multimode lasing spectrum at 160 mW incident pump power is shown in the inset.

The inset in Fig. 8 clearly shows the multimode behavior of this laser cavity. The FSR of this MML cavity is 53 GHz (0.19 nm). Any of the lasing modes can be used for sensing by heterodyning it with an external laser as shown in Fig. 6(b). The Toptica tunable laser used in this study can be tuned next to any arbitrary lasing mode resulting in one low frequency beating signal (i.e., it can be tuned within a few GHz) and many high frequencies, which fall outside the frequency detection range of the ESA employed in this study. The multimode behavior of the MML can, in principle, reduce the cost of the sensing system permitting to replace the external tunable laser to a fix wavelength laser, due to the increased probability of the external laser falling close to one of the lasing modes.

4.2. Sensing performance

In this section, the bulk refractive index sensitivity of this device is investigated. The measured LOD is an indication of the biosensing capability and it can be used to benchmark this design with other existing integrated optical sensors. Temperature noise (i.e., drift and fluctuation) is one of the biggest noise sources during sensing measurements. Therefore, the temperature coefficient of the MML cavity is also characterized.

Optics EXPRESS

4.2.1. Bulk refractive index sensing

The sensing principle is based on the variation of the lasing frequency (or wavelength) due to a change in the refractive index of the liquid cladding. The shift of the lasing frequency, one of the lasing modes, is measured by heterodyning it with an external laser as shown in Fig. 6(b). In order to achieve high temperature stability during the sensing measurements, the chip, fiber alignment stage and the flow system are covered in a box to reduce air flow around the setup and the chip holder is temperature controlled (at 26 C°) within ~±0.5 mK (standard deviation). The liquid samples are connected to a Fluigent M-switch, a flow control unit (Fluigent FRP flow-rate platform) and then into the PDMS microfluidic channel on the chip. A constant flow rate of 50 µl/min is used during the sensing experiment. The sample switch time is 280 ms (Fluigent M-switch).

The peak location of the beat note signal is measured as a function of time and it is shown in Fig. 9. The standard deviation σ (noise) without averaging is 0.96 MHz. This is a factor of ~7 smaller than the 7 MHz noise reported in our previous work [18]. This is mainly due to the reduced temperature noise (from 2.5 mK to 0.5 mK) and reduced temperature coefficient (from 1.72 GHz/K to 1.35 GHz/K, see next section). A 60 s moving window averaging (125 data points) leads to a further reduced σ of 0.19 MHz.

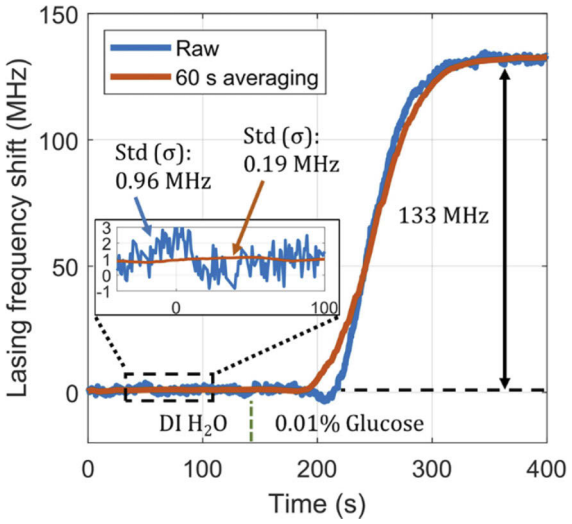

Fig. 9. Bulk refractive index sensing measured with an MML. The green vertical dashed line indicates the switch from DI water to DI water with 0.01% (weight percentage) of glucose. The lasing frequency shift starts ~70 s later, which corresponds to the time required for the liquid to flow from the switch to the MML sensor.

The lasing frequency shift, Δf, induced by 0.01% (weight percentage) glucose in DI H_2O was measured as 133 MHz. The refractive index change, Δn, between the DI H_2O and the glucose solution is 1.43×10^{-5} refractive index units (RIU) [27]. Therefore, the bulk sensitivity of this device is, $\Delta f/\Delta n$, 9.3 THz/RIU (33 nm/RIU). This is higher than the microdisk laser sensor shown in our previous work [18] due to the reduced waveguide thickness and waveguide width. Other reported sensor architectures [12] have shown higher sensitivity. However, higher sensitivity does not lead necessarily to a smaller refractive index shift detection capability (i.e., a smaller LOD). This is due to the fact that the noise is typically proportional to the sensitivity. Therefore, the LOD should be used to determine the smallest refractive index shift that can be detected.

Optics EXPRESS

The LOD in RIU is calculated as 3 times the measured noise (3σ LOD) as

$$LOD_{3\sigma} = 3\sigma \frac{\Delta n}{\Delta f}.$$

The LOD without averaging is 3.1×10^{-7} RIU. With a 60 s moving window averaging a 6.0×10^{-8} RIU is achieved. To the best of our knowledge, this is the lowest LOD measured with a microring or microdisk type of cavity [1,10,12,14,18,28–31].

4.2.2. Temperature coefficient

The effective refractive index (N_{eff}) of the waveguide mode changes with temperature since the refractive index of H_2O [32,33], Al_2O_3 [34,35] and SiO_2 [36] are a function of temperature. Thus, the cavity optical path length is also a function of temperature. Temperature induces a shift in the lasing wavelength, which in the case of a sensing device, induces thermal noise. The temperature coefficient (i.e., variation of the wavelength of the laser as a function of temperature) is measured by accurately changing the temperature of the chip (control the chip holder temperature and assume that the chip has the same temperature as the chip holder) and monitoring the beat note frequency variation. The raw data is shown in the inset of Fig. 10, where both the measured chip holder temperature, T, and the beat note frequency, f, change as a function of time are shown. The main plot in Fig. 10 replots the same data showing the beat note frequency versus temperature. A linear fit results in 1.35 GHz/K (4.8 pm/K) temperature coefficient. This value is smaller than the one reported for a microdisk laser cavity (1.72 GHz/K [18]). This is due to the smaller cross-section of the waveguide used in this work, which leads to a better-balanced overlap of the laser mode with the Al_2O_3:Yb^{3+} (positive thermal coefficient of refractive index) and the H_2O cladding (negative coefficient of refractive index), approaching a quasi athermal waveguide.

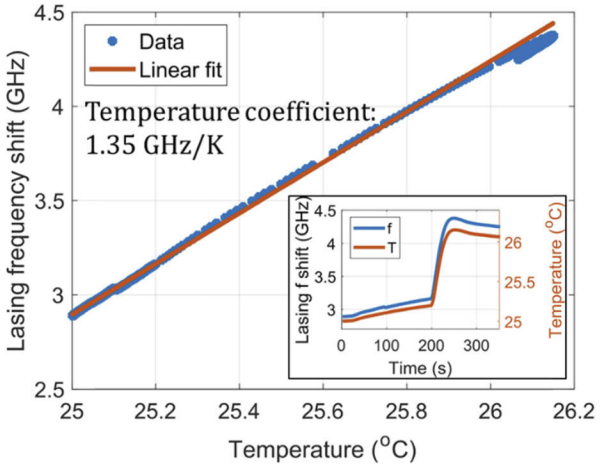

Fig. 10. Temperature coefficient of the laser frequency. The inset shows the measured chip holder temperature and the beat note frequency (beat with the external tunable laser) as a function of time. The main figure replots data in the inset with the lasing frequency shift versus the temperature. A linear fit results in 1.35 GHz/K (4.8 pm/K) temperature coefficient. Since the temperature sensor on the chip holder is very close but not at the same location as the waveguide, a small hysteresis is noticeable when the temperature starts to decrease (around 26.1 °C).

The typical temperature noise measured on the chip holder is ~±0.5 mK (standard deviation). Together with the temperature coefficient of the laser, a lasing frequency noise, σ, of ~0.68

Optics EXPRESS

MHz can be calculated. The thermal noise has, therefore, a significant contribution to the 0.96 MHz noise measured in Fig. 9. Thus, a sensor with lower LOD could be realized with a lower temperature coefficient or smaller temperature fluctuation. In principle, a cavity with negligible thermal coefficient it possible with this MML design. For example, the region 1 could be designed with a negative thermal coefficient by further reducing the width of the waveguides in region 1 (i.e., using E-beam lithography). The total thermal coefficient can be minimized by compensating the negative coefficient of region 1 with the positive thermal coefficient from region 2 and 3.

5. Conclusion and outlook

In this work, we demonstrate an MML cavity design. The aim is to dramatically improve the design and optimization ability over a traditional simple ring cavity for lasing optical and/or bio sensor. The design strategy and optimization steps has been shown in detail and implemented in an Al_2O_3:Yb^{3+} waveguide example. Due to the WDM, most of the pump power coupled to the laser cavity. Therefore, the fabricated devices have shown a 10 to 30 higher output power than simple ring designs at the same incident pump power. A bulk refractive index sensing is preformed to characterize its sensing performance. A bulk sensitivity of 9.3 THz/RIU has been measured. A noise of 0.960 MHz in the beating frequency has been measured without averaging and 0.19 MHz with a 60 s averaging (125 data points). The corresponding LOD is 3.1×10^{-7} RIU and 6.0×10^{-8} RIU, respectively. A temperature coefficient of 1.35 GHz/K has been measured. Together with the ~±0.5 mK temperature standard deviation in our chip holder, we believe the temperature fluctuation has a large contribution to our sensing noise.

The results presented here originate from the first proof-of-concept of an MML sensor in Al_2O_3:Yb^{3+}. There is still plenty of room to further optimize every section of the MML cavity in future design iterations. For instance, the bulk refractive sensitivity could be further improved by using a smaller width (i.e., using E-beam lithography) in region 1 (Fig. 1(b)). This will also reduce the temperature coefficient which leads to a smaller noise caused by temperature fluctuation. Both of these effects will lead to an even lower LOD.

Funding. Horizon 2020 Framework Programme (634928).

Disclosures. The authors declare no conflicts of interest.

References

1. X. D. Fan, I. M. White, S. I. Shopova, H. Y. Zhu, J. D. Suter, and Y. Z. Sun, "Sensitive optical biosensors for unlabeled targets: A review," Anal. Chim. Acta **620**(1-2), 8–26 (2008).
2. E. Kim, M. D. Baaske, and F. Vollmer, "Towards next-generation label-free biosensors: recent advances in whispering gallery mode sensors," Lab Chip **17**(7), 1190–1205 (2017).
3. P. Steglich, M. Hülsemann, B. Dietzel, and A. Mai, "Optical biosensors based on silicon-on-insulator ring resonators: A review," Molecules **24**(3), 519 (2019).
4. J. Su, "Label-Free Biological and Chemical Sensing Using Whispering Gallery Mode Optical Resonators: Past, Present, and Future," Sensors **17**(3), 540 (2017).
5. L. B. Shao, X. F. Jiang, X. C. Yu, B. B. Li, W. R. Clements, F. Vollmer, W. Wang, Y. F. Xiao, and Q. H. Gong, "Detection of Single Nanoparticles and Lentiviruses Using Microcavity Resonance Broadening," Adv. Mater. **25**(39), 5616–5620 (2013).
6. J. G. Zhu, S. K. Ozdemir, Y. F. Xiao, L. Li, L. N. He, D. R. Chen, and L. Yang, "On-chip single nanoparticle detection and sizing by mode splitting in an ultrahigh-Q microresonator," Nat. Photonics **4**(1), 46–49 (2010).
7. I. M. White and X. D. Fan, "On the performance quantification of resonant refractive index sensors," Opt. Express **16**(2), 1020–1028 (2008).
8. A. J. Maker and A. M. Armani, "Heterodyned toroidal microlaser sensor," Appl. Phys. Lett. **103**(12), 123302–171 (2013).
9. A. Meldrum, W. Morrish, S. Lane, W. J. Wu, T. M. Monro, and A. Francois, "Luminescent Capillary-Based Whispering Gallery Mode Sensors: Crossing the Lasing Threshold," Phys. Status Solidi A **215**(7), 1700619 (2018).
10. W. Morrish, N. Riesen, S. Stobie, A. Francois, and A. Meldrum, "Geometric Resonances for High-Sensitivity Microfluidic Lasing Sensors," Phys. Rev. Appl. **10**(5), 051001 (2018).
11. L. Q. Ren, X. W. Zhang, X. X. Guo, H. T. Wang, and X. Wu, "High-Sensitivity Optofluidic Sensor Based on Coupled Liquid-Core Laser," IEEE Photonics Technol. Lett. **29**(8), 639–642 (2017).

Optics EXPRESS

12. T. Reynolds, N. Riesen, A. Meldrum, X. D. Fan, J. M. M. Hall, T. M. Monro, and A. Francois, "Fluorescent and lasing whispering gallery mode microresonators for sensing applications," Laser Photonics Rev. **11**(2), 1600265 (2017).
13. J. Yang and L. J. Guo, "Optical sensors based on active microcavities," IEEE J. Sel. Top. Quantum Electron. **12**(1), 143–147 (2006).
14. X. W. Zhang, L. Q. Ren, X. Wu, H. Li, L. Y. Liu, and L. Xu, "Coupled optofluidic ring laser for ultrahigh-sensitive sensing," Opt. Express **19**(22), 22242–22247 (2011).
15. E. H. Bernhardi, K. O. van der Werf, A. J. Hollink, K. Wörhoff, R. M. de Ridder, V. Subramaniam, and M. Pollnau, "Intra-laser-cavity microparticle sensing with a dual-wavelength distributed-feedback laser," Laser Photonics Rev. **7**(4), 589–598 (2013).
16. M. de Goede, L. Chang, M. Dijkstra, and S. M. García-Blanco, "Integrated Al2O3: Yb3+ Microring Laser for On-Chip Active Sensing in an Aqueous Environment," ECIO 2018 (2018).
17. M. De Goede, L. Chang, M. Dijkstra, R. Obregón, J. Ramón-Azcón, E. Martínez, L. Padilla, J. Adan, F. Mitjans, and S. M. García-Blanco, "Al2O3 Microresonator Based Passive and Active Biosensors," in *2018 20th International Conference on Transparent Optical Networks (ICTON)*, (IEEE, 2018), pp. 1–4.
18. M. de Goede, L. Chang, J. Mu, M. Dijkstra, R. Obregón, E. Martínez, L. Padilla, F. Mitjans, and S. M. Garcia-Blanco, "Al2O3:Yb3+ integrated microdisk laser label-free biosensor," Opt. Lett. **44**(24), 5937–5940 (2019).
19. B. Min, T. J. Kippenberg, L. Yang, K. J. Vahala, J. Kalkman, and A. Polman, "Erbium-implanted high-Q silica toroidal microcavity laser on a silicon chip," Phys. Rev. A **70**(3), 033803 (2004).
20. C. Roeloffzen, R. de Ridder, and A. Driessen, "Low-loss adiabatic bend using minimised chip area," in *Proceedings 2000 IEEE/LEOS Symposium Benelux Chapter*, (Delft University of Technology, 2000), pp. 175–178.
21. T. Chen, H. Lee, J. Li, and K. J. Vahala, "A general design algorithm for low optical loss adiabatic connections in waveguides," Opt. Express **20**(20), 22819–22829 (2012).
22. L. Chrostowski, J. Flueckiger, C. Lin, M. Hochberg, J. Pond, J. Klein, J. Ferguson, and C. Cone, "Design methodologies for silicon photonic integrated circuits," Proc. SPIE **8989**, 89890G (2014).
23. Z. Hu and Y. Y. Lu, "Computing optimal waveguide bends with constant width," J. Lightwave Technol. **25**(10), 3161–3167 (2007).
24. R. N. Sheehan, S. Horne, and F. H. Peters, "The design of low-loss curved waveguides," Opt. Quantum Electron. **40**(14-15), 1211–1218 (2008).
25. C. I. van Emmerik, M. Dijkstra, M. de Goede, L. T. Chang, J. F. Mu, and S. M. Garcia-Blanco, "Single-layer active-passive Al2O3 photonic integration platform," Opt. Mater. Express **8**(10), 3049–3054 (2018).
26. J. D. B. Bradley, F. Ay, K. Wörhoff, and M. Pollnau, "Fabrication of low-loss channel waveguides in Al2O3 and Y2O3 layers by inductively coupled plasma reactive ion etching," Appl. Phys. B **89**(2-3), 311–318 (2007).
27. A. V. Malinin, A. A. Zanishevskaja, V. V. Tuchin, Y. S. Skibina, and I. Y. Silokhin, "Photonic crystal fibers for food quality analysis," in *Biophotonics: Photonic Solutions for Better Health Care Iii*, (International Society for Optics and Photonics, 2012), p. 842746.
28. M. de Goede, M. Dijkstra, R. Obregón, J. Ramón-Azcón, E. Martínez, L. Padilla, F. Mitjans, and S. M. Garcia-Blanco, "Al2O3 microring resonators for the detection of a cancer biomarker in undiluted urine," Opt. Express **27**(13), 18508–18521 (2019).
29. E. X. Luan, H. Shoman, D. M. Ratner, K. C. Cheung, and L. Chrostowski, "Silicon Photonic Biosensors Using Label-Free Detection," Sensors **18**(10), 3519 (2018).
30. L. Gounaridis, P. Groumas, E. Schreuder, G. Tsekenis, A. Marousis, R. Heideman, H. Avramopoulos, and C. Kouloumentas, "High performance refractive index sensor based on low Q-factor ring resonators and FFT processing of wavelength scanning data," Opt. Express **25**(7), 7483–7495 (2017).
31. A. Samusenko, D. Gandolfi, G. Pucker, T. Chalyan, R. Guider, M. Ghulinyan, and L. Pavesi, "A SiON Microring Resonator-Based Platform for Biosensing at 850 nm," J. Lightwave Technol. **34**(3), 969–977 (2016).
32. G. Abbate, U. Bernini, E. Ragozzino, and F. Somma, "The temperature dependence of the refractive index of water," J. Phys. D: Appl. Phys. **11**(8), 1167–1172 (1978).
33. A. N. Bashkatov and E. A. Genina, "Water refractive index in dependence on temperature and wavelength: a simple approximation," Proc. SPIE 5068, 393–395 (2002).
34. M. E. Thomas, S. K. Andersson, R. M. Sova, and R. I. Joseph, "Frequency and temperature dependence of the refractive index of sapphire," Infrared Phys. Technol. **39**(4), 235–249 (1998).
35. M. R. Saleem, R. Ali, S. Honkanen, and J. Turunen, "Thermal properties of thin Al2O3 films and their barrier layer effect on thermo-optic properties of TiO2 films grown by atomic layer deposition," Thin Solid Films **542**, 257–262 (2013).
36. J. Gong, R. Dai, Z. Wang, C. Zhang, X. Yuan, and Z. Zhang, "Temperature dependent optical constants for SiO2 film on Si substrate by ellipsometry," Mater. Res. Express **4**(8), 085005 (2017).